Nuclear Science and Techniques (2023) 34:91
https://doi.org/10.1007/s41365-023-01239-7

Bayesian inference of the crust–core transition density via the neutron-star radius and neutron-skin thickness data

Wen-Jie Xie[1] · **Zi-Wei Ma**[1] · **Jun-Hua Guo**[1]

Received: 18 January 2023 / Revised: 24 March 2023 / Accepted: 2 April 2023 / Published online: 24 June 2023

Abstract

In this work, we perform a Bayesian inference of the crust–core transition density ρ_t of neutron stars based on the neutron-star radius and neutron-skin thickness data using a thermodynamical method. Uniform and Gaussian distributions for the ρ_t prior were adopted in the Bayesian approach. It has a larger probability of having values higher than 0.1 fm^{-3} for ρ_t as the uniform prior and neutron-star radius data were used. This was found to be controlled by the curvature K_{sym} of the nuclear symmetry energy. This phenomenon did not occur if K_{sym} was not extremely negative, namely, $K_{sym} > -200$ MeV. The value of ρ_t obtained was $0.075^{+0.005}_{-0.01}$ fm^{-3} at a confidence level of 68% when both the neutron-star radius and neutron-skin thickness data were considered. Strong anti-correlations were observed between ρ_t, slope L, and curvature of the nuclear symmetry energy. The dependence of the three L–K_{sym} correlations predicted in the literature on crust–core density and pressure was quantitatively investigated. The most probable value of 0.08 fm^{-3} for ρ_t was obtained from the L–K_{sym} relationship proposed by Holt et al. while larger values were preferred for the other two relationships.

Keywords Crust–core transition density of neutron stars · Neutron-star radius · Neutron-skin thickness · Bayesian inference approach · L–K_{sym} correlations

1 Introduction

The determination of the crust–core transition density ρ_t in neutron stars (NSs) is important not only for predicting bulk NS properties [1] but also for the finite nucleic properties [2–4]. However, constraining the transition density remains a challenge owing to the intricate structure of the inner crust in NSs. In the past years, various theoretical models have been used to estimate the transition density. These include the dynamical method [5–9], Thomas-Fermi approximation method [10], random phase approximation [4], thermodynamical method [11–13], Vlasov method[14], compressible liquid-drop model [15] and meta-modeling approach [16]. These methods yield different predictions, namely, $\rho_t = 0.071 \pm 0.011$ fm^{-3} is estimated in the meta-modeling approach [16]; $\rho_t = 0.0955 \pm 0.0007$ fm^{-3} is obtained by comparing with the excitation energies of giant resonances, energy-weighted pygmy dipole strength, and dipole polarizability data using the relativistic nuclear energy density functionals [2]; $\rho_t = 0.04 - 0.065$ fm^{-3} is obtained using the EOS including the momentum-dependent interaction of neutron-rich nuclear matter constrained by the isospin diffusion data in heavy-ion reactions[8]; ρ_t=0.069 − 0.098 fm^{-3} is estimated from the thermodynamical method [13]; and ρ_t =0.058~0.092 fm^{-3} is determined using the Thomas-Fermi method [10]. The values predicted by the dynamical method are usually smaller than those predicted by the thermodynamical method by approximately 0.01 fm^{-3}[8].

The nuclear symmetry energy plays a dominant role in accurately describing the crust–core interface of NSs. The crust–core transition density is known to be highly sensitive to the isospin dependence of the nuclear equation of state (EOS) [1]. In particular, the slope L and curvature K_{sym} of the nuclear symmetry energy, as well as the L–K_{sym} correlation, have been reported to be strongly correlated with the

This work was supported by the Shanxi Provincial Foundation for Returned Overseas Scholars (No. 20220037), Natural Science Foundation of Shanxi Province (No. 20210302123085), and Discipline Construction Project of Yuncheng University.

✉ Wen-Jie Xie
wenjiexie@yeah.net

[1] Department of Physics, Yuncheng University, Yuncheng 044000, China

crust–core transition density [12, 15, 16]. In a recent study [15], a Bayesian approach was used to infer the distribution of ρ_t based on low-density constraints for neutrons and symmetric nuclear matter from the effective field theory. However, the obtained ρ_t distribution and correlations between ρ_t and the EOS parameters depend strongly on the surface energy parameter. In the present work, we perform a Bayesian inference of the crust–core transition density in NSs based on the NS radius and neutron-skin thickness data. The dependence of the L–K_{sym} correlations predicted in the literature on the posterior distribution of ρ_t is discussed.

The remainder of this study is organized as follows. In the next section, we outline the theoretical framework, including the thermodynamical method, EOS metamodeling method, nuclear droplet model, and Bayesian inference approach. In Sect. 3, we probe the crust–core transition density and its correlations with the EOS parameters using the NS radius and neutron- skin thickness data in the Bayesian framework. We also explore the effect of the L–K_{sym} correlation on the crust–core transition density and pressure. Finally, we summarize our results.

2 Theoretical framework

2.1 Crust–core transition density and isospin-dependent parametric EOS for the core of NSs

In the present work, the crust–core transition density was estimated by adopting the thermodynamical approach under the condition that the energy per nucleon $E(\rho,\delta)$ in nuclear matter at nucleon density ρ and isospin asymmetry $\delta \equiv (\rho_n - \rho_p)/\rho$ could be approximated by the isospin-parabolic expansion:

$$E(\rho,\delta) \approx E_0(\rho) + E_{sym}(\rho)\cdot\delta^2. \tag{1}$$

The crust–core transition point is obtained when the uniform matter starts separating into a mixture comprising single nucleons and clusters. The transition density is specifically calculated using the vanishing effective incompressibility of uniform NS matter under β equilibrium and charge-neutrality conditions:

$$K_\mu = \rho^2\frac{\mathrm{d}^2E_0}{\mathrm{d}\rho^2} + 2\rho\frac{\mathrm{d}E_0}{\mathrm{d}\rho} + \delta^2\left[\rho^2\frac{\mathrm{d}^2E_{sym}}{\mathrm{d}\rho^2} + 2\rho\frac{\mathrm{d}E_{sym}}{\mathrm{d}\rho} - 2E_{sym}^{-1}\left(\rho\frac{\mathrm{d}E_{sym}}{\mathrm{d}\rho}\right)^2\right]. \tag{2}$$

Therefore, the transition density ρ_t can be obtained by solving $K_\mu = 0$. Notably, the crust–core transition density can be overestimated when the parabolic approximation (Eq. 1) is used [8]. As shown in Fig. 5 of Ref. [8], this overestimation mainly appears in the region where the parameters L and K_{sym} are large, namely, $L > 60$ MeV and $K_{sym} > -100$ MeV. However, after filtered by the NS radius data, the probability that they fall into the above-mentioned intervals is very small, according to our earlier calculations [17]. Therefore, employing the parabolic approximation hardly changes the present results. Furthermore, it can also reduce the discrepancy between the thermodynamical method used in the present work and other approaches, such as the dynamical method, when the EOS parameters are compared with the NS radius data.

The transition pressure can be approximated as [18]

$$P_t \approx \frac{K_0}{9}\frac{\rho_t^2}{\rho_0}\left(\frac{\rho_t}{\rho_0} - 1\right) + \rho_t\delta_t\left[\frac{1-\delta_t}{2}E_{sym}(\rho_t) + \left(\rho\frac{dE_{sym}(\rho)}{d\rho}\right)_{\rho_t}\delta_t\right], \tag{3}$$

where δ_t is isospin asymmetry corresponding to ρ_t. E_0 and E_{sym} in Eqs. (1) and (2) are the energy per particle in symmetric nuclear matter (SNM) and nuclear symmetry energy, respectively. They can be parameterized as

$$E_0(\rho) = E_0(\rho_0) + \frac{K_0}{2}\left(\frac{\rho-\rho_0}{3\rho_0}\right)^2 + \frac{J_0}{6}\left(\frac{\rho-\rho_0}{3\rho_0}\right)^3, \tag{4}$$

$$E_{sym}(\rho) = E_{sym}(\rho_0) + L\left(\frac{\rho-\rho_0}{3\rho_0}\right) + \frac{K_{sym}}{2}\left(\frac{\rho-\rho_0}{3\rho_0}\right)^2 + \frac{J_{sym}}{6}\left(\frac{\rho-\rho_0}{3\rho_0}\right)^3, \tag{5}$$

where $E_0(\rho_0) = -15.9$ MeV is the energy per particle at the saturation density ρ_0 for SNM. $K_0 = 9\rho_0^2[\partial^2E_0(\rho)/\partial\rho^2]|_{\rho=\rho_0}$ and $J_0 = 27\rho_0^3[\partial^3E_0(\rho)/\partial\rho^3]|_{\rho=\rho_0}$ represent the incompressibility and skewness parameters of SNM at ρ_0, respectively. Furthermore, $E_{sym}(\rho_0)$, $L = 3\rho_0[\partial E_{sym}(\rho)/\partial\rho]|_{\rho=\rho_0}$, $K_{sym} = 9\rho_0^2[\partial^2E_{sym}(\rho)/\partial\rho^2]|_{\rho=\rho_0}$, and $J_{sym} = 27\rho_0^3[\partial^3E_{sym}(\rho)/\partial\rho^3]|_{\rho=\rho_0}$ denote the magnitude, slope, curvature, and skewness of nuclear symmetry energy at ρ_0, respectively. According to the systematics of terrestrial nuclear experiments and predictions of various nuclear theories, K_0, $E_{sym}(\rho_0)$, and L have the ranges of 220–260 MeV, 28.5–34.9 MeV, and 30–90 MeV [19–23], respectively. Based only on theoretical predictions [24, 25], the parameters J_0, K_{sym}, and J_{sym} characterizing the nuclear EOS at high densities have wide ranges of $-800 \le J_0 \le 400$ MeV, $-400 \le K_{sym} \le 100$ MeV, and $-200 \le J_{sym} \le 800$ MeV, respectively.

In the framework of the minimum NS model, the non-rotating NS comprises neutrons, protons, electrons, and muons under β equilibrium and charge neutrality

conditions, and the relationship between the pressure and nucleon density in the core of NSs

$$P(\rho,\delta)=\rho^2\frac{\mathrm{d}\epsilon(\rho,\delta)/\rho}{\mathrm{d}\rho} \tag{6}$$

is controlled by the energy density $\epsilon(\rho,\delta)=\rho[E(\rho,\delta)+M_{\mathrm{N}}]+\epsilon_l(\rho,\delta)$. Here, M_{N} and $\epsilon_{\mathrm{l}}(\rho,\delta)$ denote the average nucleon mass and energy densities for leptons which are calculated by the noninteracting Fermi gas model[26], respectively. δ can be obtained using the charge neutrality condition $\rho_{\mathrm{p}}=\rho_{\mathrm{e}}+\rho_{\mu}$ and the β-equilibrium condition $\mu_{\mathrm{n}}-\mu_{\mathrm{p}}=\mu_{\mathrm{e}}=\mu_{\mu}\approx 4\delta E_{\mathrm{sym}}(\rho)$, where μ denotes the chemical potential calculated by the expression $\mu_i=\partial\epsilon(\rho,\delta)/\partial\rho_i$ for the ith particle.

The EOS for the core of the NSs can be constructed in terms of (4), (5), and (6). Below the crust–core transition density, the NV EOS [27] and BPS EOS [1] were employed for the inner and outer crusts, respectively.

2.2 Neutron skin and nuclear droplet model

The neutron-skin thickness of a finite nucleus in the nuclear droplet model (DM) is obtained according to the following expression [3, 28]:

$$\Delta R_{\mathrm{np}}=\sqrt{\frac{3}{5}}\left[t-\frac{e^2Z}{70E_{\mathrm{sym}}(\rho_0)}+\frac{5}{2R}\left(b_{\mathrm{n}}^2-b_{\mathrm{p}}^2\right)\right], \tag{7}$$

where $e^2Z/70\,E_{\mathrm{sym}}(\rho_0)$ is a correction term owing to the Coulomb interaction. $R=r_0A^{1/3}$ indicates the nuclear radius, while b_{n} and b_{p} denote the surface widths of the neutron and proton density profiles, respectively. $b_{\mathrm{n}}=b_{\mathrm{p}}=1$ fm is usually used in the standard DM. The quantity t in Eq. (7) is calculated as[3]

$$t=\frac{2r_0}{3E_{\mathrm{sym}}(\rho_0)}L\left(1-x\frac{K_{\mathrm{sym}}}{2L}\right)xA^{1/3}(\delta-\delta_C) \tag{8}$$

with

$$x=\frac{\rho_0-\rho_A}{3\rho_0},\delta_C=\frac{e^2Z}{20E_{\mathrm{sym}}(\rho_0)R}. \tag{9}$$

Here, $\rho_A=0.1$ fm^{-3} and $\rho_A=0.08$ fm^{-3} for the ^{208}Pb and ^{48}Ca nuclei, respectively.

2.3 Bayesian inference approach

The Bayesian theorem is expressed as

$$P(\mathcal{M}|D)=CP(D|\mathcal{M})P(\mathcal{M}) \tag{10}$$

where C is a normalization constant. $P(\mathcal{M}|D)$ denotes the obtained posterior probability distribution function (PDF) of the model $\mathcal{M}$ when the dataset D is provided. $P(D|\mathcal{M})$ is a likelihood function obtained by comparing the theoretical results from model $\mathcal{M}$ with data D, and $P(\mathcal{M})$ is the prior probability of model $\mathcal{M}$ representing knowledge of the theoretical parameters of $\mathcal{M}$ before comparison with data D.

In the present work, we randomly sampled the transition density in the range of 0.03 fm $^{-3}\le\rho_{\mathrm{t}}\le$ 0.2 fm $^{-3}$, and the matched six-parameter set was determined by solving the equation $K_{\mu}=0$ using Eq. (2). Two methods were adopted to generate the posterior PDF of the transition density. One was based only on the observed data of the NS radii, while the other was based on both the NS radius data and neutron-skin thickness data. In the first method, we used the six matched parameters to construct the NS EOS in the framework of the minimum NS model, as described above, and substitute them in the TOV equation to compute the theoretical values of the NS radii. We then obtained the likelihood of the transition density or the matched set of parameters by comparing the theoretical values of the NS radii with the observed values using the following likelihood function:

$$P(D|\mathcal{M})=\frac{1}{\sqrt{2\pi}\sigma}\exp\left[-\frac{(R_{\mathrm{th}}-R_{\mathrm{obs}})^2}{2\sigma^2}\right]. \tag{11}$$

Here, R_{th} is the theoretical values while R_{obs} and σ represent the observed values and 1σ error bar for the NS radii, respectively. The NS EOS generated above should satisfy the thermodynamical stability condition ($\mathrm{d}P/\mathrm{d}\epsilon\ge 0$, where P is the pressure inside NSs) and the causality condition ($0\le v_{\mathrm{s}}^2\le c^2$, v_{s} and c denote the speed of sound and light, respectively) at all densities, and should be stiff enough to support the maximum mass of the NS observed thus far. A sharp cut-off of 1.97 $\mathrm{M}_{\odot}$ was used in this analysis.

In the second method, the matched six-parameter set was obtained using Eq. (2) by sampling the transition density. We then set as the input to the DM to calculate the theoretical values of the neutron-skin thickness for ^{208}Pb and ^{48}Ca. We discarded these parameter sets and transition densities when the calculated values for the neutron-skin thickness were far from the experimental values using the following likelihood function:

$$P(D|\mathcal{M})=\frac{1}{\sqrt{2\pi}\sigma'}\exp\left[-\frac{(\Delta R_{\mathrm{np}}^{\mathrm{th}}-\Delta R_{\mathrm{np}}^{\mathrm{exp}})^2}{2\sigma'^2}\right]. \tag{12}$$

Here $\Delta R_{\mathrm{np}}^{\mathrm{th}}$ and $\Delta R_{\mathrm{np}}^{\mathrm{exp}}$ are the theoretical and experimental values, respectively, and σ' represents the 1σ error bars for the experimental data. Subsequently, the remaining parameter sets were used to construct the NS EOS and estimate the posterior PDFs of the transition density, as described above.

The observed data for the NS radii and experimental data for the neutron-skin thickness used in this study are summarized in Table 1. These NS data include: (i) $R_{1.4} = 11.9^{+1.4}_{-1.4}$ km at 90% confidence level (CFL) by analyzing the GW170817 source reported by the LIGO/Virgo Collaboration [29]; (ii) $R_{1.4} = 10.8^{+2.1}_{-1.6}$ km at 90% CFL by analyzing the same source of GW170817 [30]; (iii) $R_{1.4} = 11.7^{+1.1}_{-1.1}$ km at 90% CFL reported earlier by analyzing the quiescent low-mass X-ray binaries (QLMXBs) [31]; (iv) Reported by the NICER Collaboration [33, 36] at 68% CFL, $R = 12.71^{+1.14}_{-1.19}$ with mass of $1.34^{+0.15}_{-0.16}M_\odot$ [32] and $R = 13.02^{+1.24}_{-1.06}$ with mass of $1.44^{+0.15}_{-0.14}M_\odot$ [36] for the source of PSR J0030+0451, $R = 13.7^{+2.6}_{-1.5}$ with mass of $2.08^{+0.07}_{-0.07}M_\odot$ for the source of PSR J0740+6620. The data for the neutron-skin thickness were $\Delta R_{\rm np} = 0.121^{+0.026}_{-0.026}$ fm and $\Delta R_{\rm np} = 0.283^{+0.071}_{-0.071}$ fm for ^{48}Ca and ^{208}Pb, respectively, which were obtained from Refs. [34, 35] recently reported by the CREX and PREX-2 Collaborations.

The Metropolis-Hastings algorithm within a Markov chain Monte Carlo (MCMC) approach was adopted to generate the posterior PDFs of the model parameters. The PDFs of the individual parameters and the PDFs for the two-parameter correlations were calculated by integrating over all other parameters using the marginal estimation approach. The initial samples in the so-called burn-in period were discarded [37] so that the MCMC process started from an equilibrium distribution. In the present analysis, 40,000 steps and the remaining one million steps were used for the burn-in progress and for calculating the PDF of the transition density, respectively.

3 Results and discussions

3.1 Exploring the crust–core transition density via NS observations

The posterior PDFs of the crust–core transition density ρ_t, corresponding transition pressure P_t, and their correlations with the EOS coefficients are plotted in Fig. 1. Two types of priors for ρ_t were adopted in the calculations. The first form is a uniform distribution, which is a better choice because we have no information about ρ_t. This is illustrated by the black curves in Fig. 1. The second form, which is indicated by the purple curve in Fig. 1, is a Gaussian distribution with an average value of 0.078 fm^{-3} and standard deviation of 0.04, as in. [3]. The panels located in the two upper rows show the posterior PDFs of the correlations mentioned above using uniform priors for ρ_t. The panels in the two bottom rows show the results obtained using the Gaussian priors. These results are based only on the observed data of the NS radii, as summarized in Table 1.

A two-humped posterior distribution for ρ_t was observed for both the uniform and Gaussian priors used in the calculations. The first peak which is located at $\rho_t = 0.08$ fm^{-3}, is often used as a fiducial value in the literature. The second peak is located at $\rho_t = 0.1$ fm^{-3}. The 68 % and 90 % credible intervals calculated using the highest posterior density interval approach for ρ_t and P_t are listed in Table 2. Relative to the prior distributions, the posterior PDFs of ρ_t narrow down to small intervals, which indicates that the crust–core transition density is sensitive to the NS radius. It has a higher probability of falling into the region where the values of ρ_t exceed 0.1 fm^{-3} when an uninformative prior is used. This can be attributed to the correlations between ρ_t and some EOS parameters, which will be discussed later.

A better constraint on ρ_t was found when the Gaussian prior was used in comparison with those using the uniform prior. It is easy to understand that more information is available for the Gaussian prior than for the uniform prior before comparing them with the NS radius data. The generated ranges of P_t, namely, $0.05^{+1.25}_{-0.04}$ MeV/fm^3 using the uniform prior and $0.1^{+0.28}_{-0.1}$ MeV/fm^3 using the Gaussian prior at the 68% confidence level, as listed in Table 2, covered those calculated using the meta-modelling, dynamical, and thermodynamical models, as shown in Table I in Ref. [15]. However, the most probable values are smaller than them. Our results for ρ_t are consistent with those in literature.

Table 1 Data for the NS radius and neutron-skin thickness used in the present work

Mass($M_\odot$)	Radius R (km)	Source and Reference
1.4	$11.9^{+1.4}_{-1.4}$(90% CFL)	GW170817 [29]
1.4	$10.8^{+2.1}_{-1.6}$ (90% CFL)	GW170817 [30]
1.4	$11.7^{+1.1}_{-1.1}$ (90% CFL)	QLMXBs [31]
$1.34^{+0.15}_{-0.16}$	$12.71^{+1.14}_{-1.19}$ (68% CFL)	PSR J0030+0451 [32]
$1.44^{+0.15}_{-0.14}$	$13.0^{+1.2}_{-1.0}$ (68% CFL)	PSR J0030+0451 [33]
$2.08^{+0.07}_{-0.07}$	$13.7^{+2.6}_{-1.5}$ (68% CFL)	PSR J0740+6620 [33]
Nucleus	ΔR_{np} (fm)	Source and Reference
^{48}Ca	$0.121^{+0.026}_{-0.026}$(68% CFL)	CREX[34]
^{208}Pb	$0.283^{+0.071}_{-0.071}$(68% CFL)	PREX-2[35]

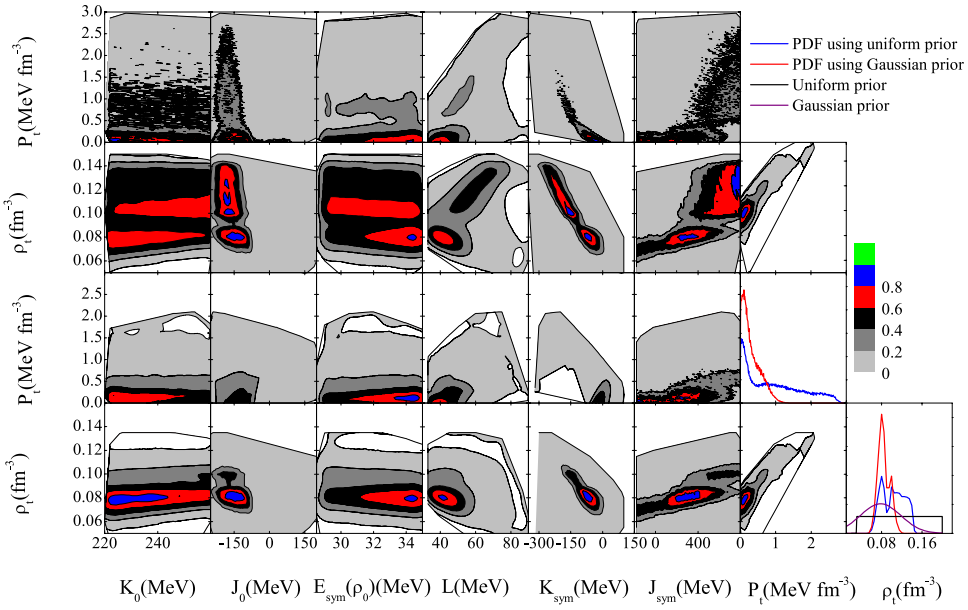

Fig. 1 (Color online) Posterior PDFs of the crust–core transition density and pressure as well as their correlations with the EOS parameters. The calculations are performed by adopting the uniform (blue curves) and Gaussian (red curves) priors for the transition density based on the NS radius data. For comparison, the uniform (black curve) and Gaussian (purple curve) forms for the prior distributions of the transition density are included. The correlations in the two upper (bottom) rows are calculated by using the uniform (Gaussian) prior for the transition density

Table 2 Most probable values and the 68% and 90% credible intervals of ρ_t and P_t calculated by using the uniform prior, Gaussian prior, neutron-star plus neutron-skin thickness data (NS+NST), $L-K_{\rm sym}$ correlation in Ref. [38] by Holt et al. $L-K_{\rm sym}$ correlation in Ref. [39] by Mondal et al., and $L-K_{\rm sym}$ correlation in Ref. [24] by Tews et al.

	Uniform prior	Gaussian prior	NS+NST	Holt et al. [38]	Mondal et al. [39]	Tews et al. [24]
ρ_t	$0.08^{+0.06}_{-0.005}$,$0.08^{+0.06}_{-0.025}$	$0.08^{+0.01}_{-0.03}$,$0.08^{+0.025}_{-0.03}$	$0.075^{+0.005}_{-0.01}$,$0.075^{+0.025}_{-0.01}$	$0.08^{+0.005}_{-0.005}$,$0.08^{+0.01}_{-0.015}$	$0.1^{+0.005}_{-0.01}$,$0.1^{+0.01}_{-0.02}$	$0.1^{+0.005}_{-0.01}$,$0.1^{+0.01}_{-0.02}$
P_t	$0.05^{+1.25}_{-0.04}$,$0.05^{+2.13}_{-0.04}$	$0.1^{+0.28}_{-0.1}$,$0.1^{+0.6}_{-0.1}$	$0.1^{+0.2}_{-0.08}$,$0.1^{+0.64}_{-0.08}$	$0.16^{+0.01}_{-0.06}$,$0.16^{+0.18}_{-0.08}$	$0.6^{+0.18}_{-0.14}$,$0.6^{+0.28}_{-0.28}$	$0.6^{+0.18}_{-0.14}$,$0.6^{+0.28}_{-0.26}$

We explored the correlations among $\rho_{\rm t}$, $P_{\rm t}$, and the EOS parameters. Here, we did not consider the correlations between the EOS parameters, which were consistent with those reported in our previous publications[17, 40]. Low-order parameters such as $E_{\rm sym}(\rho_0)$ and K_0 were barely correlated with the transition. However, as mentioned in Refs. [12], the condition $K_\mu = 0$ required a larger $\rho_{\rm t}$ as K_0 increased. This phenomenon is observed in Fig. 1, where a weak positive correlation is observed between $\rho_{\rm t}$ and K_0 when both the uniform and Gaussian priors are used.

Strong correlations among $\rho_{\rm t}$ and the isovector compressibility $K_{\rm sym}$, skewness $J_{\rm sym}$ were discovered, which was consistent with the results reported in Refs. [16]. The negative correlation between $\rho_{\rm t}$ and $K_{\rm sym}$ was inconsistent with the results of Ref. [16], in which the EOS parameters were filtered by the predictions from the effective field theory and surface coefficients were determined by the nuclear masses in the framework of the extended Thomas Fermi approximation method. The positive correlations between $\rho_{\rm t}$ and $J_{\rm sym}$ and $\rho_{\rm t}$ and $P_{\rm t}$ (shown in Fig. 1) are consistent with those reported in Ref. [15, 16]. The transition was unaffected by the skewness of the symmetric nuclear matter, J_0.

L exhibited a negative correlation with $\rho_{\rm t}$. Interestingly, a positive correlation appeared in the region $\rho_{\rm t} > 0.1\,{\rm fm}^{-3}$ when the uniform prior was used; however, this did not occur when the Gaussian prior was used. Is this related to the shoulder indicated in the posterior PDF of ρ_t using the uniform prior in Fig. 1, ? To answer this question, we plot the L–$K_{\rm sym}$ correlations from the three types of calculations, as indicated in Fig. 2, namely, using the uniform and Gaussian priors based on the NS radius data, and the uniform prior based on both the NS radius and neutron-skin thickness data. Two phenomena are observed in Fig. 2. They are the anti-correlation shown in the left and right panels, and the very weak correlation shown in the middle panel between L and $K_{\rm sym}$, as shown in the left panel in Fig. 2, $K_{\rm sym}$ has a high probability to stay in the region where $K_{\rm sym}$ is extremely negative, i.e. $K_{\rm sym} <$ -200 MeV. The latter is clearly responsible for the shoulder because the shoulder for the posterior PDF of ρ_t disappears, as shown in Fig. 3 although the L–$K_{\rm sym}$ anti-correlations are the same in their calculations in the left and right panels. Therefore, $K_{\rm sym}$ plays a more important role in constraining the crust–core transition density of NSs than the

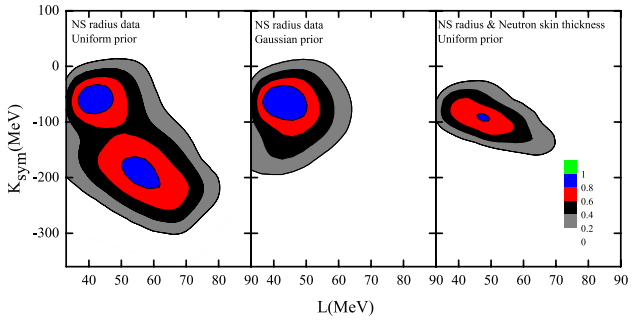

Fig. 2 (Color online) Correlations between L and $K_{\rm sym}$ calculated from the NS radius data using the uniform (left) and Gaussian (middle) priors, and from both the neutron-star radius and neutron-skin thickness data (right) using the uniform prior

L–$K_{\rm sym}$ correlation, as studied in Ref. [12]. The transition pressure was weakly correlated with the EOS parameters.

3.2 Effect of the neutron-skin thickness and comparison with other calculations

The neutron-skin thickness is known to be an effective probe for nuclear symmetry energy, especially its slope parameter [41, 42]. The latter plays an important role in determining the crust–core transition density of NSs. The results presented in Fig. 3 are the same as those in Fig. 1 but based on both the NS radius data and neutron-skin thickness data. In the calculations, we first performed a Bayesian inference of the coefficients $E_{\rm sym}(\rho_0)$, L and $K_{\rm sym}$ within the framework of the nuclear droplet model, as described in Sec. 2.2 based on the neutron-skin thickness data reported by the CREX [34] and PREX-2 [35] Collaborations as listed in Table 1. Subsequently, we regarded the obtained distributions of these parameters and the matched transition density as their priors to infer the posterior PDF of the transition density based on the NS radius data within the minimum NS model. Notably, there is a significant controversy regarding constraining the slope of the symmetry energy through the neutron-skin thickness data of ^{48}Ca and ^{208}Pb reported by the CREX and PREX-2 Collaborations. A recent study demonstrated that the ranges of the slope L obtained from CREX and PREX-2 were completely inconsistent [43]. Therefore, more accurate measurements are required. Fortunately, there are methods for determining the neutron-skin thickness, such as the configurational information entropy analysis [44, 45].

As seen in Fig. 3, the correlations are roughly same as those in Fig. 1. A weak anti-correlation between the symmetry energy magnitudes $E_{\rm sym}(\rho_0)$ and $\rho_{\rm t}$ was observed, owing to the constraint from the neutron-skin thickness data on $E_{\rm sym}(\rho_0)$. The range for $K_{\rm sym}$ is smaller than that obtained using only the NS radius data, which is also because of the effect of the neutron-skin thickness data. The constraint on ρ_t obtained is improved in comparison with those based only on NS data, as listed in Table 2 because the parameters L and $K_{\rm sym}$ are better constrained when the neutron-skin thickness data are considered.

In Fig. 4 we compare our results with those inferred using a compressible liquid-drop model within a Bayesian framework [15], which employs two filters, namely, the low density (LD) behavior of the energy functionals that should be rigorously limited in the uncertainty intervals of the effective field theory calculations for symmetric and pure neutron matter [46] and the high density (HD) behavior of the functionals that should obey the conditions such as positive symmetry energy at all densities and causality [15]. Our results were consistent with theirs. There $P_{\rm t}$ had a long tail for when the uniform prior was used in the calculations, because a large probability of $\rho_{\rm t}$ existed in the region at $\rho_{\rm t} > 0.1$ fm^{-3}. The most probable values of $P_{\rm t}$ obtained in this study were smaller than those in Ref. [15].

3.3 Effect of L–$K_{\rm sym}$ correlations

As L–$K_{\rm sym}$ correlations significantly affect both the crust–core transition density and pressure [12]. To further explore this effect, we considered three typical L-$K_{\rm sym}$ correlations predicted in the literature as the priors to infer the posterior PDF of ρ_t. For completeness and ease of

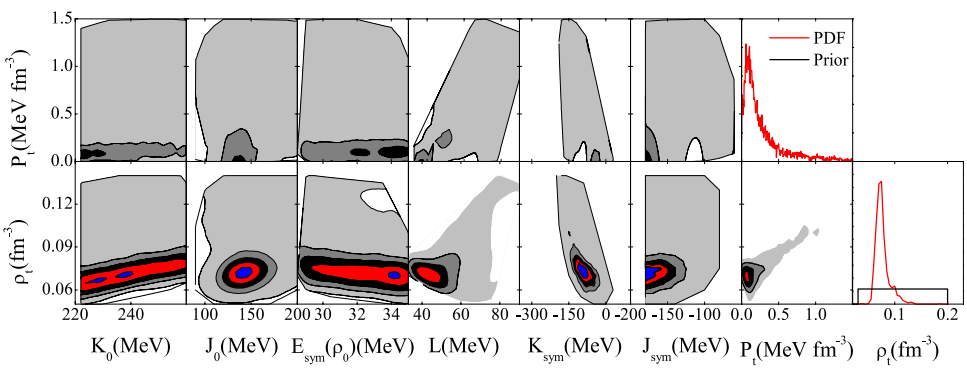

Fig. 3 (Color online) Posterior PDFs of the crust–core transition density and pressure and their correlations with the EOS parameters. In the calculations, both the neutron-skin thickness and NS radius data are adopted. The prior distribution (black curve) for the transition density is included

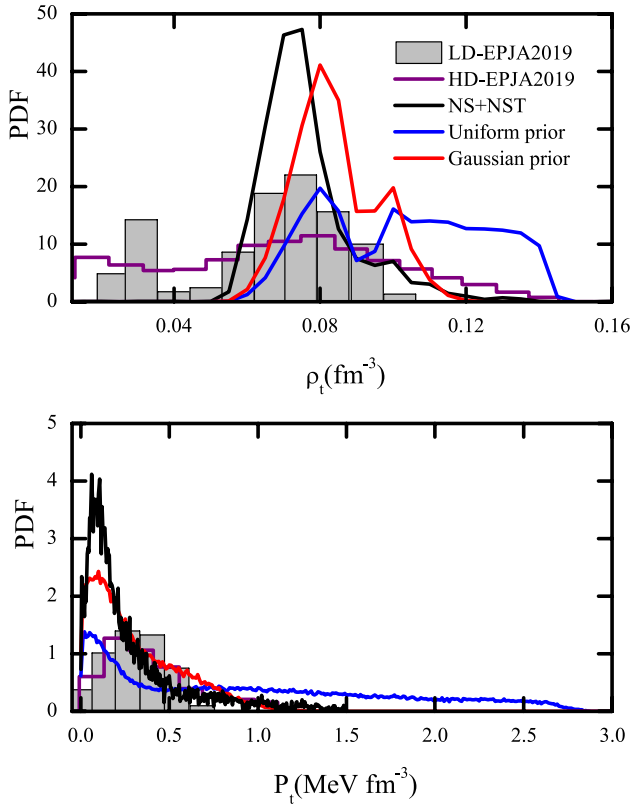

Fig. 4 (Color online) Posterior PDFs of the crust–core transition density and pressure based on only the NS radius data using the uniform (blue curve) and Gaussian (red curve) priors, and based on both the NS radius and neutron-skin thickness data using the uniform prior indicated by NS+NST (black curve). The results presented in Ref. [15] shown by LD-EPJA2019 and HD-EPJA2019 are included for comparison

discussions, we briefly describe the three correlations. The first one is based on the theoretical predictions from 240 Skyrme Hartree-Fock and 263 relativistic mean-field calculations [39] by Mondal et al. and written as

$$K_{\rm sym} = (-4.97 \pm 0.07)(3E_{\rm sym}(\rho_0) - L) + 66.80 \pm 2.14\,{\rm MeV}. \quad (13)$$

The second was obtained from Ref. [24] by Tews et al. and written as

$$K_{\rm sym} = 3.50L - 305.67 \pm 24.26\,{\rm MeV}. \quad (14)$$

In the framework of the Fermi liquid theory, Holt and Lim [38] derived the expressions $L = 6.70E_{\rm sym}(\rho_0) - 148.60 \pm 4.37$ MeV and $K_{\rm sym} = 18.50E_{\rm sym}(\rho_0) - 613.18 \pm 9.62$ MeV. Thus, we can formulate the last relationship between L and $K_{\rm sym}$ as [12]

$$K_{\rm sym} = 2.76L - 203.07 \pm 21.69\,{\rm MeV}. \quad (15)$$

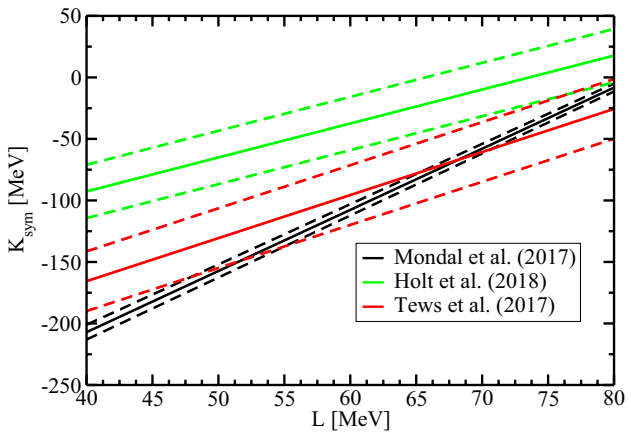

Fig. 5 (Color online) $L - K_{\rm sym}$ correlations from Tews et al. [24] (red curves), Mondal et al. [39] (black curves), and Holt et al. [38] (green curves). The solid and dashed lines denote the mean values and boundaries of each correlation, respectively. Adapted from Ref. [12]

The correlations are shown in Fig. 5. The discrepancy between the correlations obtained by Mondal et al. and Tews et al. is not very large because they are from the same sets of theoretical predictions. However, the results shown in Figs. 2 and 5 differ significantly. This illustrates that the L–$K_{\rm sym}$ correlations are strongly model-dependent, and constraining them has a long way to go.

In the Bayesian inference approach, after considering the abovementioned correlations, L and $K_{\rm sym}$ were no longer independent when we randomly sampled them between their specific ranges. The uniform prior for ρ_t and only the NS radius data were employed in the calculations performed in this subsection. The generated posterior PDFs for ρ_t and P_t are presented in Fig. 6, and the corresponding confidence intervals are summarized in Table 2. As stated in Refs. [12], the $L - K_{\rm sym}$ correlations play a significant role in constraining both the transition density and pressure. We observe that: (i) The results from the relations by Mondal et al. and Tews et al. were completely consistent primarily because these two correlations largely overlapped within the allowed error limits. (ii)The most probable values obtained from the relations by Holt et al. differed significantly from the other two cases. For the latter, the transition density and pressure were larger than those for the former because $K_{\rm sym}$ was not extremely negative in the relationship by Holt et al., that is, $K_{\rm sym}$, with values higher than approximately -115 MeV as shown by the green curves in Fig. 5. The present results are consistent with those reported in Ref. [12], in which the authors studied the effects of $L - K_{\rm sym}$ correlations on the crust–core transition density and pressure by adopting fixed values of the other parameters in Eqs. (4) and (5).

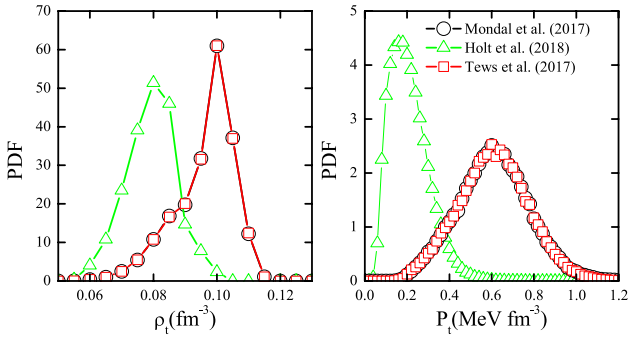

Fig. 6 (Color online) Posterior PDFs of the crust–core transition density and pressure as the three correlations of $L - K_{\rm sym}$ as in Fig. 5 are used in the calculations

4 Summary

In summary, Bayesian inference of the crust–core transition density based on the NS radius and neutron-skin thickness data was performed using the thermodynamical approach to calculate the crust–core transition density and an explicitly isospin-dependent parametric EOS for the core of NSs within the minimum NS model. Uniform and Gaussian forms of the prior distributions of the transition density were employed in the calculations. The transition density had a higher probability of taking values larger than 0.1 fm^{-3} when the uniform prior was used, which did not occur when a the Gaussian prior was used. This phenomenon was attributed to values of $K_{\rm sym}$ which were smaller than -200 MeV.

Negative (positive) correlations between $\rho_{\rm t}$ and L and $\rho_{\rm t}$ and $K_{\rm sym}$ (between $\rho_{\rm t}$ and K_0, between ρ_t and $J_{\rm sym}$ and between $\rho_{\rm t}$ and $P_{\rm t}$) were observed. Based on the NS radius data reported thus far, the 68 % confidence intervals generated for ρ_t were $0.08^{+0.06}_{-0.005}$ fm^{-3} and $0.08^{+0.01}_{-0.03}$ fm^{-3} when uniform and Gaussian priors were adopted, respectively. When the EOS parameters were first filtered using the neutron-skin thickness data, a value of $0.075^{+0.005}_{-0.01}$ fm^{-3} was obtained. We also checked the impact of L–$K_{\rm sym}$ correlations on the posterior PDFs of $\rho_{\rm t}$ and $P_{\rm t}$. The results from the L–$K_{\rm sym}$ relationships reported by Tews et al. [24] and Mondal et al.[39] completely overlapped, whereas those reported by Holt et al. [38] were smaller than those obtained from the other two L–$K_{\rm sym}$ relations.

Author contributions All authors contributed to the study conception and design. Material preparation, data collection and analysis were performed by Wen-Jie Xie, Zi-Wei Ma and Jun-Hua Guo. The first draft of the manuscript was written by Wen-Jie Xie and all authors commented on previous versions of the manuscript. All authors read and approved the final manuscript.

Data availability The data that support the findings of this study are openly available in Science Data Bank at https://www.doi.org/[https://doi.org/10.57760/sciencedb.08231 and https://cstr.cn/[https://cstr.cn/31253.11.sciencedb.08231.

Declarations

Conflict of interest The authors declare that they have no competing interests.

References

1. G. Baym, C. Pethick, P. Sutherland, The ground state of matter at high densities: equation of state and stellar models. Astrophys. J. **170**, 299 (1971). https://doi.org/10.1086/151216
2. N. Paar, C.C. Moustakidis, T. Marketin et al., Neutron star structure and collective excitations of finite nuclei. Phys. Rev. C **90**, 011304 (2014). https://doi.org/10.1103/PhysRevC.90.011304
3. M. Centelles, X. Roca-Maza, X. Vinas et al., Nuclear symmetry energy probed by neutron skin thickness of nuclei. Phys. Rev. Lett. **102**, 122502 (2009). https://doi.org/10.1103/PhysRevLett.102.122502
4. C. Horowitz, J. Piekarewicz, Neutron star structure and the neutron radius of ^{208}pb. Phys. Rev. Lett. **86**, 5647 (2001). https://doi.org/10.1103/PhysRevLett.86.5647
5. L. Tsaloukidis, C. Margaritis, C.C. Moustakidis, Effects of the equation of state on the core-crust interface of slowly rotating neutron stars. Phys. Rev. C **99**, 015803 (2019). https://doi.org/10.1103/PhysRevC.99.015803
6. J. Fang, H. Pais, S. Pratapsi et al., Crust-core transition of a neutron star: effects of the symmetry energy and temperature under strong magnetic fields. Phys. Rev. C **95**, 062801 (2017). https://doi.org/10.1103/PhysRevC.95.062801
7. C. Gonzalez-Boquera, M. Centelles, X. Viñas et al., Core-crust transition in neutron stars with finite-range interactions: the dynamical method. Phys. Rev. C **100**, 015806 (2019). https://doi.org/10.1103/PhysRevC.100.015806
8. J. Xu, L.W. Chen, B.A. Li et al., Nuclear constraints on properties of neutron star crusts. Astrophys. J. **697**, 1549 (2009). https://doi.org/10.1088/0004-637X/697/2/1549
9. J.M. Lattimer, Y. Lim, Constraining the symmetry parameters of the nuclear interaction. Astrophys. J. **771**, 51 (2013). https://doi.org/10.1088/0004-637X/771/1/51
10. S.S. Bao, H. Shen, Impact of the symmetry energy on nuclear pasta phases and crust-core transition in neutron stars. Phys. Rev. C **91**, 015807 (2015). https://doi.org/10.1103/PhysRevC.91.015807
11. C.C. Moustakidis, Effect of the symmetry energy on the location of the inner edge of the neutron star crust. Phys. Rev. C **86**, 015801 (2012). https://doi.org/10.1103/PhysRevC.86.015801
12. B.A. Li, M. Magno, Curvature-slope correlation of nuclear symmetry energy and its imprints on the crust-core transition, radius, and tidal deformability of canonical neutron stars. Phys. Rev. C **102**, 045807 (2020). https://doi.org/10.1103/PhysRevC.102.045807
13. Z.W. Liu, Z. Qian, R.Y. Xing et al., Nuclear fourth-order symmetry energy and its effects on neutron star properties in the relativistic Hartree-Fock theory. Phys. Rev. C **97**, 025801 (2018). https://doi.org/10.1103/PhysRevC.97.025801
14. H. Pais, A. Sulaksono, B.K. Agrawal et al., Correlation of the neutron star crust-core properties with the slope of the symmetry energy and the lead skin thickness. Phys. Rev. C **93**, 045802 (2016). https://doi.org/10.1103/PhysRevC.93.045802

15. T. Carreau, F. Gulminelli, J. Margueron, Bayesian analysis of the crust-core transition with a compressible liquid-drop model. Eur. Phys. J. A **55**, 188 (2019). https://doi.org/10.1140/epja/i2019-12884-1
16. S. Antić, D. Chatterjee, T. Carreau et al., Quantifying the uncertainties on spinodal instability for stellar matter through meta-modeling. J. Phys. G Nucl. Part. Phys. **46**, 065109 (2019). https://doi.org/10.1088/1361-6471/ab1a51
17. W.J. Xie, B.A. Li, Bayesian inference of high-density nuclear symmetry energy from radii of canonical neutron stars. Astrophys. J. **883**, 174 (2019). https://doi.org/10.3847/1538-4357/ab3f37
18. J.M. Lattimer, M. Prakash, Neutron star observations: prognosis for equation of state constraints. Phys. Rep. **442**, 109–165 (2007). https://doi.org/10.1016/j.physrep.2007.02.003
19. P. Danielewicz, R. Lacey, W.G. Lynch, Determination of the equation of state of dense matter. Science **298**, 1592–1596 (2002). https://doi.org/10.1126/science.1078070
20. S. Shlomo, V. Kolomietz, G. Colo, Deducing the nuclear-matter incompressibility coefficient from data on isoscalar compression modes. Eur. Phys. J. A Hadrons Nucl. **30**, 23–30 (2006). https://doi.org/10.1140/epja/i2006-10100-3
21. J. Piekarewicz, Do we understand the incompressibility of neutron-rich matter? J. Phys. G Nucl. Part. Phys. **37**, 064038 (2010). https://doi.org/10.1088/0954-3899/37/6/064038
22. B.A. Li, X. Han, Constraining the neutron-proton effective mass splitting using empirical constraints on the density dependence of nuclear symmetry energy around normal density. Phys. Lett. B **727**, 276–281 (2013). https://doi.org/10.1016/j.physletb.2013.10.006
23. M. Oertel, M. Hempel, T. Klähn et al., Equations of state for supernovae and compact stars. Rev. Mod. Phys. **89**, 015007 (2017). https://doi.org/10.1103/RevModPhys.89.015007
24. I. Tews, J.M. Lattimer, A. Ohnishi et al., Symmetry parameter constraints from a lower bound on neutron-matter energy. Astrophys. J. **848**, 105 (2017). https://doi.org/10.3847/1538-4357/aa8db9
25. N.B. Zhang, B.J. Cai, B.A. Li et al., How tightly is the nuclear symmetry energy constrained by a unitary fermi gas? Nucl. Sci. Tech. **28**, 181 (2017). https://doi.org/10.1007/s41365-017-0336-2
26. N.B. Zhang, B.A. Li, J. Xu, Combined constraints on the equation of state of dense neutron-rich matter from terrestrial nuclear experiments and observations of neutron stars. Astrophys. J. **859**, 90 (2018). https://doi.org/10.3847/1538-4357/aac027
27. J.W. Negele, D. Vautherin, Neutron star matter at sub-nuclear densities. Nucl. Phys. A **207**, 298–320 (1973). https://doi.org/10.1016/0375-9474(73)90349-7
28. M. Warda, X. Vinas, X. Roca-Maza et al., Neutron skin thickness in the droplet model with surface width dependence: indications of softness of the nuclear symmetry energy. Phys. Rev. C **80**, 024316 (2009). https://doi.org/10.1103/PhysRevC.80.024316
29. B.P. Abbott, R. Abbott, T. Abbott et al., Gw170817: measurements of neutron star radii and equation of state. Phys. Rev. Lett. **121**, 161101 (2018). https://doi.org/10.1103/PhysRevLett.121.161101
30. S. De, D. Finstad, J.M. Lattimer et al., Tidal deformabilities and radii of neutron stars from the observation of GW170817. Phys. Rev. Lett. **121**, 091102 (2018). https://doi.org/10.1103/PhysRevLett.121.091102
31. J.M. Lattimer, A.W. Steiner, Constraints on the symmetry energy using the mass-radius relation of neutron stars. Eur. Phys. J. A **50**, 1–24 (2014). https://doi.org/10.1140/epja/i2014-14040-y
32. T.E. Riley, A.L. Watts, S. Bogdanov et al., A nicer view of PSR J0030+ 0451: millisecond pulsar parameter estimation. Astrophys. J. Lett. **887**, L21 (2019). https://doi.org/10.3847/2041-8213/ab481c
33. E. Fonseca, H.T. Cromartie, T.T. Pennucci et al., Refined mass and geometric measurements of the high-mass PSR J0740+ 6620. Astrophys. J. Lett. **915**, L12 (2021). https://doi.org/10.3847/2041-8213/ac03b8
34. D. Adhikari, H. Albataineh, D. Androic et al., Precision determination of the neutral weak form factor of Ca 48. Phys. Rev. Lett. **129**, 042501 (2022). https://doi.org/10.1103/PhysRevLett.129.042501
35. D. Adhikari, H. Albataineh, D. Androic et al., Accurate determination of the neutron skin thickness of Pb 208 through parity-violation in electron scattering. Phys. Rev. Lett. **126**, 172502 (2021). https://doi.org/10.1103/PhysRevLett.126.172502
36. M.C. Miller, F. Lamb, A. Dittmann et al., The radius of PSR J0740+ 6620 from nicer and XMM-newton data. Astrophys. J. Lett. **918**, L28 (2021). https://doi.org/10.3847/2041-8213/ac089b
37. R. Trotta, *Bayesian methods in cosmology*. arXiv preprint arXiv:1701.01467 . https://doi.org/10.48550/arXiv.1701.01467
38. J.W. Holt, Y. Lim, Universal correlations in the nuclear symmetry energy, slope parameter, and curvature. Phys. Lett. B **784**, 77–81 (2018). https://doi.org/10.1016/j.physletb.2018.07.038
39. C. Mondal, B. Agrawal, J. De et al., Interdependence of different symmetry energy elements. Phys. Rev. C **96**, 021302 (2017)
40. W.J. Xie, B.A. Li, Bayesian inference of the symmetry energy of superdense neutron-rich matter from future radius measurements of massive neutron stars. Astrophys. J. **899**, 4 (2020). https://doi.org/10.3847/1538-4357/aba271
41. J. Xu, Constraining isovector nuclear interactions with giant dipole resonance and neutron skin in 208Pb from a Bayesian approach. Chin. Phys. Lett. **38**, 042101 (2021). https://doi.org/10.1088/0256-307X/38/4/042101
42. J. Xu, W.J. Xie, B.A. Li, Bayesian inference of nuclear symmetry energy from measured and imagined neutron skin thickness in Sn 116, 118, 120, 122, 124, 130, 132, Pb 208, and Ca 48. Phys. Rev. C **102**, 044316 (2020). https://doi.org/10.1103/PhysRevC.102.044316
43. S. Tagami, T. Wakasa, M. Yahiro, Slope parameters determined from CREX and PREX2. Results Phys. **43**, 106037 (2022). https://doi.org/10.1016/j.rinp.2022.106037
44. H.L. Wei, X. Zhu, C. Yuan, Configurational information entropy analysis of fragment mass cross distributions to determine the neutron skin thickness of projectile nuclei. Nucl. Sci. Tech. **33**, 111 (2022). https://doi.org/10.1007/s41365-022-01096-w
45. C.W. Ma, Y.P. Liu, H.L. Wei et al., Determination of neutron-skin thickness using configurational information entropy. Nucl. Sci. Tech. **33**, 6 (2022). https://doi.org/10.1007/s41365-022-00997-0
46. C. Drischler, K. Hebeler, A. Schwenk, Asymmetric nuclear matter based on chiral two- and three-nucleon interactions. Phys. Rev. C **93**, 054314 (2016). https://doi.org/10.1103/PhysRevC.93.054314